Supporting Information: Vibrational Dynamics and Couplings of the Hydrated RNA Backbone – a 2D-IR Study

Eva M. Bruening, Jakob Schauss, Torsten Siebert, Benjamin P. Fingerhut, Thomas Elsaesser

Max-Born-Institut für Nichtlineare Optik und Kurzzeitspektroskopie, D-12489 Berlin, Germany

1. Experimental methods and data analysis

Sample preparation. Double stranded RNA oligomers containing 23 alternating adenine-uracil base pairs (supplier Integrated DNA Technologies) and their sodium counterions were dissolved in bulk H_2O (concentration 10^{-2} M). The sample cell in the 2D-IR experiments consisted of two 1-mm thick BaF_2 windows and a spacer of 6 μm thickness. All measurements were performed in a transmission geometry with the sample at ambient temperature (T=295 K). Comparative experiments were performed with double stranded DNA oligomers consisting of 23 alternating adenine-thymine base pairs in Watson-Crick geometry and the sugar-phosphate backbones. DNA samples with a 10^{-2} M concentration in H_2O were prepared and studied under the same conditions as the RNA samples.

Two-dimensional infrared (2D-IR) experiments. The 2D-IR spectra were measured in 3-pulse photon echo experiments with a heterodyne detection of the nonlinear signal. The 3 mid-infrared pulses interacting with the sample and the local oscillator pulse for heterodyne detection had a duration of 120 fs and pulse energies on the order of 1 μJ. They were generated in a parametric frequency converter driven by the output of an amplified Ti:sapphire laser system working at a 1 kHz repetition rate. Details of pulse generation and the setup of the photon echo experiment have been presented in refs. 1-3. Two sets of measurements were performed with pulses centered at 1030 and 1160 cm^{-1}. The intensity spectra of the pulses are shown in Fig. S1.

The heterodyned photon echo signal was spectrally dispersed and detected by a 64-element HgCdTe array (spectral resolution 2 cm^{-1}), thus providing the detection frequency ν_3 in the 2D spectra. The excitation frequency ν_1 was derived by Fourier transforming signals measured for different coherence times τ between the first two pulses along τ. In Figs. 2 and 3 of the article, the absorptive 2D signal, i.e., the real part of the sum of the rephasing and nonrephasing third-order signal is plotted as a function of ν_1 and ν_3.[4] The amplitudes of the different peaks in the 2D spectra were not corrected for the spectral intensity profile $I(\nu) \propto |E(\nu)|^2$ of the femtosecond pulses.

Mid-infrared pump-probe measurements. The 2D-IR experiments were complemented by temporally and spectrally resolved pump-probe measurements in order to determine the decay times of the v=1 states of the different backbone vibrations. Pump and probe pulses of 130 fs duration were generated in an optical parametric amplifier driven by 800 nm pulses from a Ti:sapphire laser system working at a 1 kHz repetition rate. The pump pulses of 0.5 μJ energy were focused to a spot diameter of some 200 μm on the samples and the resulting transmission changes were measured by a probe pulse in reference to a third pulse passing an unexcited part of the sample. The energies of probe and reference pulses were less than 0.5% of the pump energy. The transmitted probe and reference pulses were detected with a monochromator and a 64-pixel HgCdTe double-array detector (spectral resolution 1.5 cm^{-1}). Details of the pump-probe setup have been presented in ref. 5.

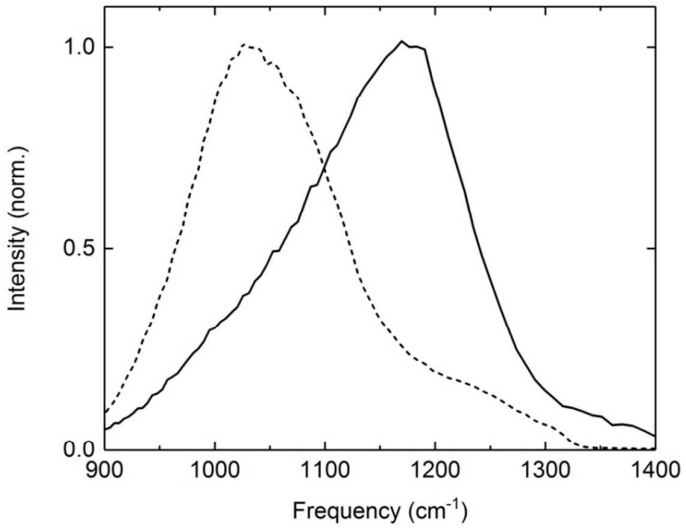

Fig. S1. Intensity spectra $I(\nu) \propto |E(\nu)|^2$ of the femtosecond pulses in the 2D-IR experiments.

Analysis of 2D spectra. The experimental 2D spectra were analyzed by calculating the third-order response functions to the photon-echo pulse sequence by a perturbative density matrix approach of light-matter interaction, including Kubo lineshape analysis and the lifetime broadening caused by the population relaxation of the different vibrations. A detailed description of this treatment has been given in the extended supplement of Ref. 1. Simulations were performed for the 2D spectra recorded at a waiting time T=250 fs. The fluctuating forces originating from the aqueous environment and RNA structure fluctuations are included via the frequency fluctuation correlation function (FFCF). The linear infrared absorption spectrum of RNA was calculated as a benchmark, making use of the parameters extracted from the analysis of the 2D spectra.

The frequency fluctuation correlation function is given by the Kubo ansatz,

$$\left\langle \delta\nu_i(t)\delta\nu_i(0)\right\rangle = \Delta_{1,i}^2 \exp(-t/\tau_1) + \Delta_{2,i}^2 \exp(-t/\tau_2)$$

where $\delta\nu_i(t)$ represents the frequency excursion of mode *i* at time *t* from its average transition frequency, $\Delta_{1,i}$ and $\Delta_{2,i}$ are fluctuation amplitudes, and τ_1 and τ_2 the related correlation times. The lineshapes of all diagonal peaks at the different hydration levels were reproduced by keeping the values of τ_1 = 300 fs and τ_2 = 50 ps constant and adjusting the amplitudes $\Delta_{1,i}$ and $\Delta_{2,i}$ for each mode. The slow component causes a quasi-static inhomogeneous broadening.

2. Two-dimensional (2D) infrared spectra

A series of 2D spectra was measured for different waiting times T to assess a reshaping of the 2D lineshapes by spectral diffusion. Spectra measured up to a waiting time T=1500 fs are summarized in Fig. S2 for the lower (left column) and higher (right column) frequency range. The absorptive 2D signals are normalized to the maximum positive signals in the spectra recorded at T=500 fs. Within the experimental accuracy, changes in the 2D lineshapes of the diagonal peaks are minor while their intensity decreases with increasing T due to the population decay of the v=1 levels of the different modes. The vibrational lifetimes cover a range from 0.3 to 2 ps, resulting in a change of relative intensity of the peaks within a particular 2D spectrum.

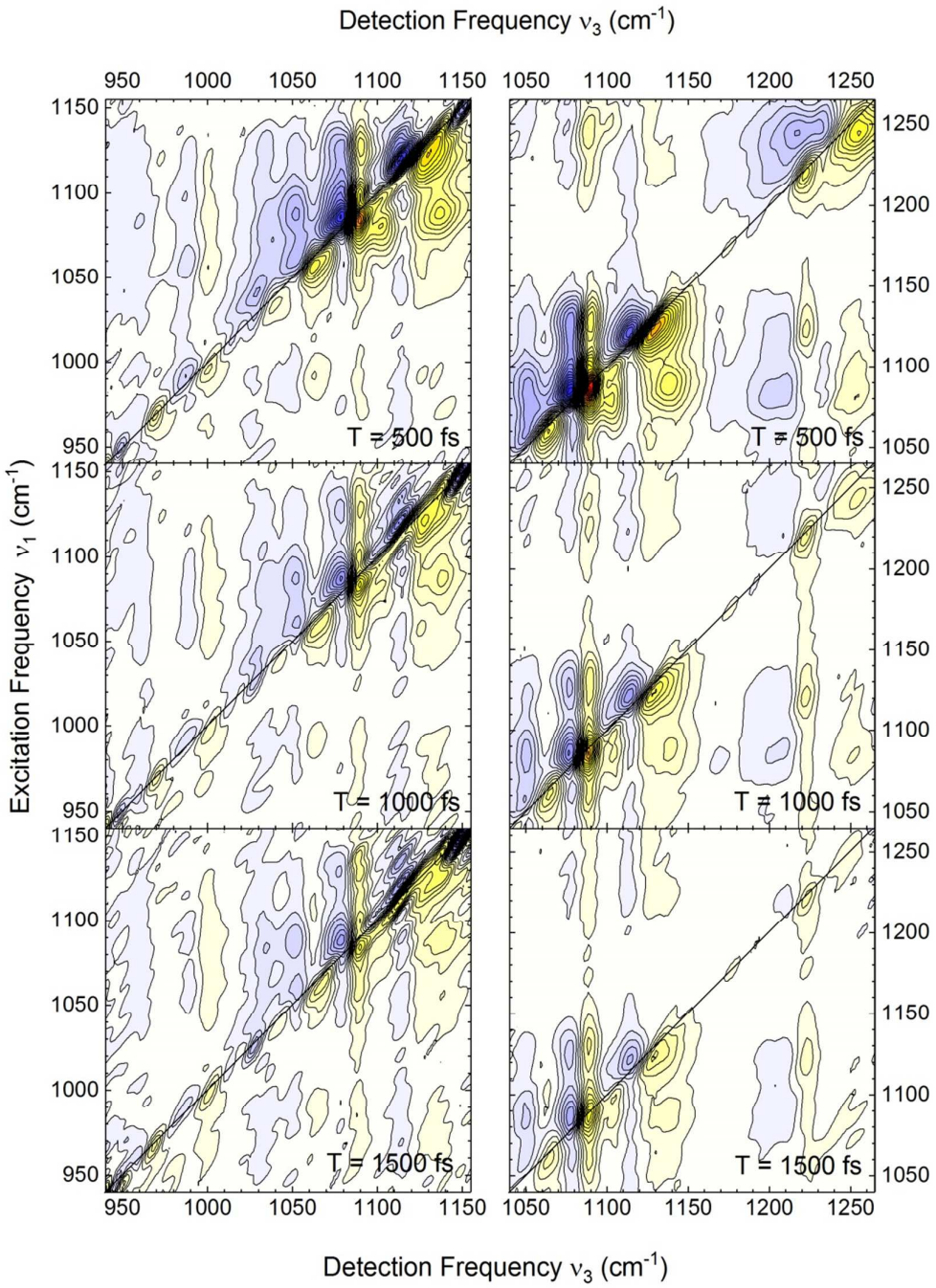

Fig. S2. Two-dimensional infrared spectra of RNA recorded for different waiting times T.

In Fig. S3, we compare experimental data with results from the numerical analysis based on density matrix and Kubo lineshape theory. Fig. S3 shows the linear infrared spectrum of the RNA sample (solid line, cf. Fig. 1b of the article) and the absorption spectra calculated with the parameters extracted from the 2D spectra (dashed line), both normalized to the peak absorbance at 1087 cm^{-1}. The lineshapes and frequency positions of the different absorption bands are well reproduced by the calculation whereas there are discrepancies in the relative intensity of the different bands. The latter originate from the fact that the peak intensities in the 2D spectra are not corrected for the spectral electric field profiles $E(\omega)$ of the femtosecond pulses (cf. Fig. S1) and, thus, are weighted with $|E(\nu)|^4$. The calculated spectrum normalized

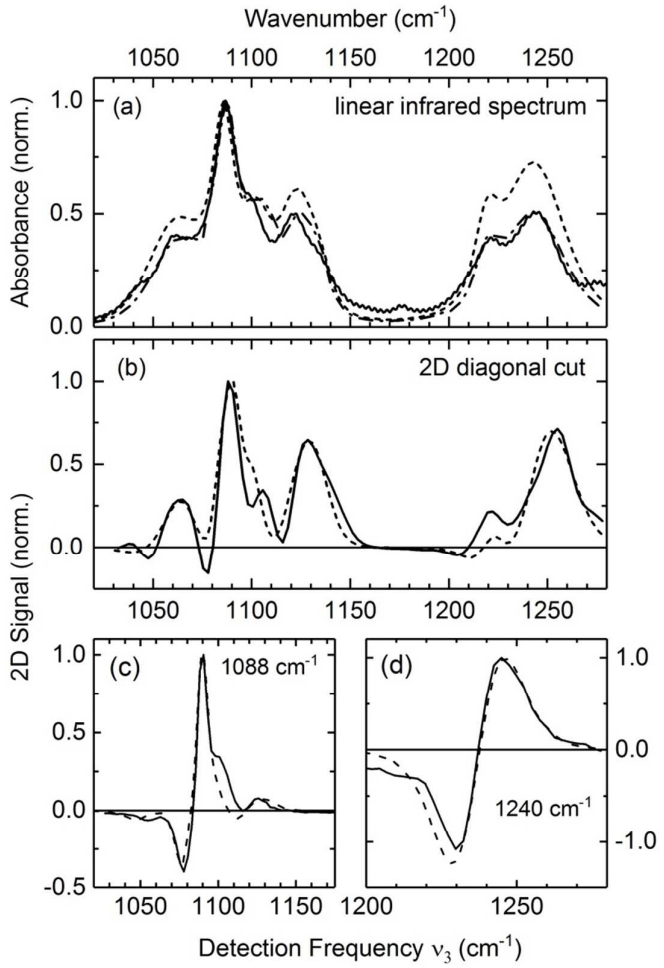

Fig. S3. Linear absorption spectrum and cuts of 2D spectra. Solid lines represent experimental data, dashed lines give results of calculations. The antidiagonal cuts were taken at (c) ν_1=1088 cm^{-1} and (d) ν_1=1240 cm^{-1}.

to the individual peak heights of the experimental spectrum (dash-dotted line in Fig. S3a) underlines the good agreement between experimental and calculated lineshapes.

DNA oligomers containing 23 alternating adenine-thymine (AT) base pairs in Watson Crick geometry were studied under the same hydration conditions as the RNA oligomers. While both RNA and DNA display 2D diagonal peaks of the symmetric and asymmetric $(PO_2)^-$ stretching modes, the number and character of the other backbone modes is different in the two systems (cf. Fig. 3 of the article). The experimental 2D spectra of DNA were analyzed with the same approach as the RNA spectra, using identical time constants τ_1=300 fs and τ_2=50 ps in the frequency fluctuation correlation function. The amplitudes Δ_1 and Δ_2 for the two $(PO_2)^-$ stretching modes of DNA are given in parentheses in Table 1 of the article.

3. Pump-probe results

Temporally and spectrally resolved pump-probe measurements were performed in parallel to the 2D experiments. Pump-probe spectra for different delay times are presented in Fig. S4 for a range of probe frequencies from (a) 1060 to 1145 cm^{-1} and (b) 1170 to 1280 cm^{-1}. The negative changes of absorbance are due to ground state bleaching and stimulated emission on

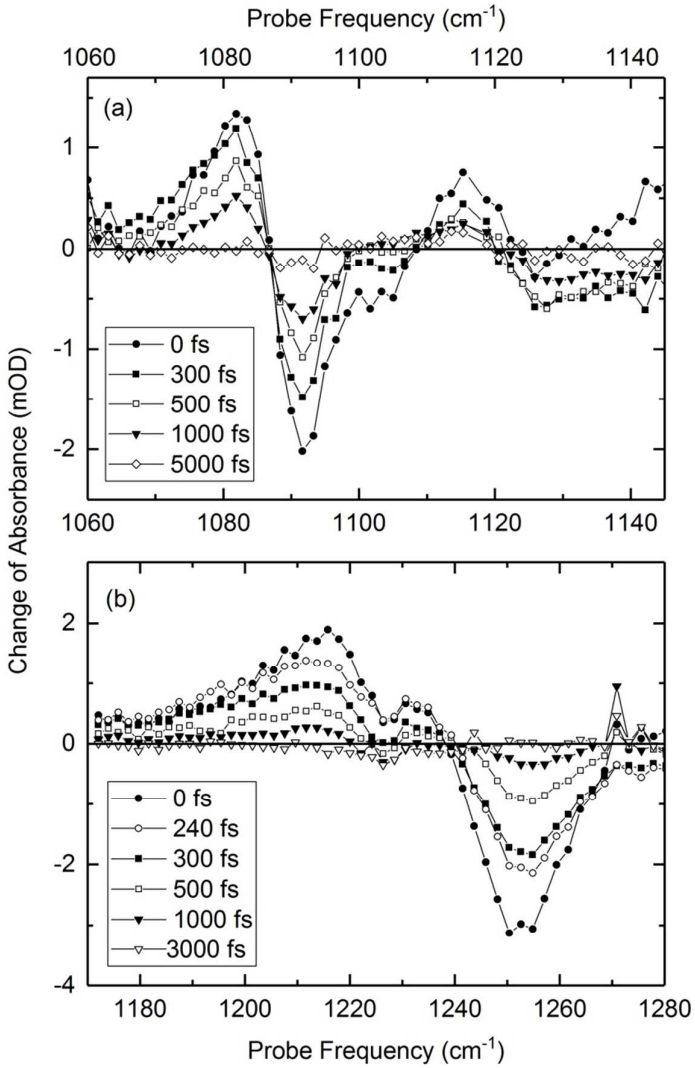

Fig. S4. Pump-probe spectra of RNA for different delay times. The change of absorbance $\Delta A=-log(T/T_0)$ is plotted as a function of probe frequency (T, T_0: sample transmission with and without excitation).

the v=0 to 1 transition whereas the positive absorbance changes reflect the transient v=1 to 2 absorption. The spectral overlap of such two components from the different backbone vibrations results in highly congested pump-probe spectra in which the different fundamental v=0 to 1 transitions are discerned only in part.

Figure S5 shows selected pump-probe transients recorded at fixed probe frequencies in the range of (a,b) the symmetric and (c,d) asymmetric $(PO_2)^-$ stretching vibration. At positive delay times, the transients display a decay to zero within a few picoseconds, i.e., long-lived signals due to vibrational heating are essentially absent. For extracting v=1 lifetimes of the vibrations, the time-dependent absorption decrease on the v=0 to 1 transitions was fitted by exponential kinetics to derive the v=1 lifetime (solid lines). The fitting curves start at a positive pump-probe delay of 300 fs after which contributions from the Kerr effect in the liquid sample and from coherent pump-probe coupling are negligible. The extracted time constants are listed in Table 1 of the article. The lifetimes of 1.0 and 0.36 ps of the symmetric and asymmetric $(PO_2)^-$ stretching modes are similar to their lifetimes in DNA and phospholipids.[1,5] Lifetimes for the ribose C-O-C stretching and the $C_{2'\text{-}OH}$ stretching mode

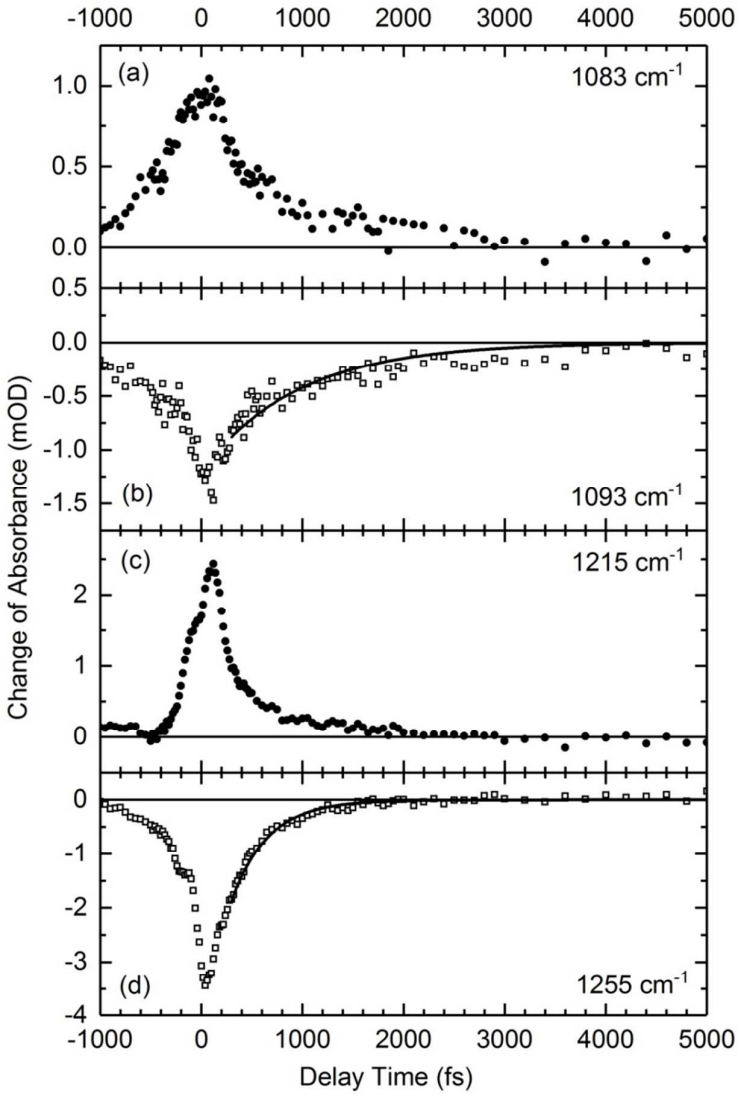

Fig. S5. Time-resolved pump-probe transients recorded at the fixed probe frequencies given in the individual panels. The solid lines are exponential fitting curves to the data.

were derived from the pump-probe data in a similar way (cf. Table 1). For all other modes, the pump-probe spectra are too congested for a reliable extraction of their lifetimes. In the theoretical simulations of the 2D infrared spectra, we assumed a lifetime of 1 ps for such modes.

4. Theoretical methods

Molecular Dynamics (MD) simulations. An initial model structure of a AU 23-mer RNA double strand (A-form, sequence: 5'-UUAUAUAUAUAUAUAUAUAUAUU-3' and its complementing strand) was generated with the nucleic acid builder (NAB) of the AmberTools program suite as canonical Watson-Crick A-RNA double helix. The starting model structure was placed in a truncated octahedral solvation box with 10.0 Å buffer region. We consider three model setups: Setup **A** employs the SPC/E water model and sodium counterions were added for charge neutrality (44 Na^+) by placing ions at positions of high electrostatic potential (*addions* command). In Setup **B** (SPC/E water) solvent molecules more than 4.0 Å away from the A-RNA helix are randomly replaced by 44 sodium counterions (*addIonsRand* command).

Further, in Setup **C** the TIP3P water model is employed with random replacement of water molecules by 44 sodium counterions for charge neutrality. As a result of the different neutralization procedures counter ions in Setup **A** are initially located in the vicinity of negatively charged $(PO_2)^-$ groups, and statistically distributed within the simulation box in Setup **B** and **C**. MD simulations were performed with AMBER 14[6] employing the *ff*99bsc0 force field with χ_{OL3} corrections[7] as recommended for RNA. Ion parameters for the SPC/E and TIP3P water model, respectively, were taken from Refs. 8,9. Simulations have been performed with the PMEMD program and the GPU (Tesla K80) accelerated PMEMD.CUDA program.[10,11]

Molecular dynamics was performed in the NPT ensemble (pressure 1.0 bar, 2 ps pressure relaxation time, Langevin dynamics with 1 ps collision frequency for temperature regulation) with a time step of 2 fs and SHAKE bond length constraints on bonds involving hydrogen atoms. Periodic boundary conditions are imposed with electrostatic interactions evaluated with the particle mesh Ewald method employing a cut-off for long range interactions of 10.0 Å. Coordinates are written to file every 250 time steps (0.5 ps).

Equilibration was performed by initial minimization of solvent and ion molecules, restraining atomic positions of the RNA double helix (harmonic constraints 500.0 kcal/mol $Å^{-2}$, 1000 optimization steps), followed by minimization of the entire system (2500 optimization steps). Subsequent short MD (20 ps) was performed to gradually heat the system to 300 K with weak harmonic position restraints on RNA duplex (10 kcal/mol $Å^{-2}$), followed by 200 ps of MD without applying positions restraints in the NPT ensemble (pressure 1 bar) for density equilibration. The first 39.4 ns of the production run (NPT ensemble) were further discarded as equilibration period. Subsequent production runs cover in total 0.6 μs of simulation time (200 ns for each Setup). Geometries for the evaluation of normal mode frequencies in QM/MM simulations (see below) were taken every 20 ns.

Quantum mechanical molecular mechanics (QM/MM) normal mode analysis. Combined QM/MM simulations have been performed with the NWChem program package, v. 6.3.[12] Along the RNA double helix backbone a single phosphate group together with the two adjacent ribose moieties (33 atoms) were treated on QM level in each simulation. Hydrogen link atoms have been employed for bonds crossing the boundary between quantum and classical regions. The first two residues at the 5' and 3' ends of the helix have been discarded resulting in 36 QM/MM simulations along the helix per MD snapshot (1188 QM/MM normal mode analysis in total). QM/MM calculations have been performed with the B3LYP exchange correlation functional along with Grimme's DFT-D3 dispersion correction[13] and 6-311+G* basis set for phosphorous atoms and the 6-31G* basis for all other atoms (C, N, O, H). All point charges within a radius of 15.0 Å around the QM region were allowed to interact with the quantum region, both electrostatically and through Van der Waals interactions.
Normal mode analysis of the QM region was performed subsequent to optimization of the QM region subject to interactions with the MM region. For geometric changes due to optimization we find a mean RMSD of 0.235 Å with standard deviation σ = 0.067 Å. The respective heavy atom mean RMSD is 0.160 Å (σ = 0.054 Å). Accordingly, changes of QM region geometries due to optimization are minor and reflect the differences in MM and QM force fields as well as relaxation to the instantaneous local minima imposed by solvent and RNA A-helix environment. A detailed analysis will be given in a forthcoming publication. A Lorentzian linewidth of $d\nu$ = 3.5 cm^{-1} has been employed for the simulation of IR signals.

Data analysis and vibrational mode assignment. Figure S6 shows major groove width (defined as shortest inter-strand P…P distance), the number of $(PO_2)^-$ … H_2O and $(PO_2)^-$ … Na^+ hydrogen bonds (defined as $P{=}O_{1/2}$ …X distance < 3.2 or 3.5 Å with X= H_2O and Na^+,

respectively) and instantaneous vibrational frequencies of asymmetric $(PO_2)^-$ modes ν_{P1} as function of base step location along the RNA helix at 120 ns simulation time (solid lines). Mean values (blue dashed) and respective standard deviation σ (red and yellow dashed) have been recorded by averaging over a 40 ns period (100-140 ns). We find that the majority of ν_{P1} are substantially blue shifted compared to the experimental value (1220 – 1240 cm^{-1}) while at distinct $(PO_2)^-$ sites good agreement with experiment is obtained (e.g. base step #8: 1237 cm^{-1}). Similar behavior is found for all investigated snapshots. Such values of ν_{P1} in the range ~ 1220 – 1260 cm^{-1} indicate fully solvated $(PO_2)^-$ groups, confirmed by ~ 6-7 $(PO_2)^-$ … H_2O hydrogen bonds formed on average. Further, we find a strong anti-correlation of $(PO_2)^-$ … Na^+ hydrogen bond number and P1 normal mode frequency ν_{P1} where the pronounced solvatochromic sensitivity of the P1 mode is reflected by blue shifted vibrational frequencies (ν_{P1} > 1280 cm^{-1}). Similarly, the $(PO_2)^-$ … H_2O hydrogen bond number is reduced if Na^+ counterions are in close contact with the $(PO_2)^-$ group due to replacement of water molecules in the first solvation shell. Regions of narrow major groove width (#9-11) are found to correlate with high local ion populations.

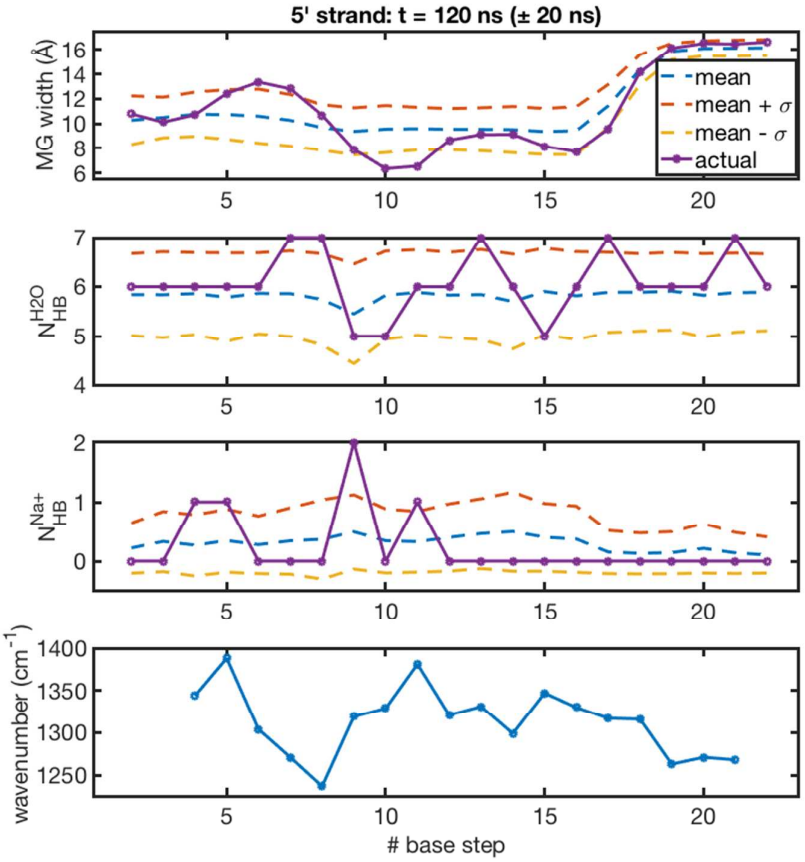

Fig. S6. Major groove width (top), number of $(PO_2)^-$… H_2O and $(PO_2)^-$… Na^+ hydrogen bonds (middle panels, $N^{H2O}{}_{HB}$ and $N^{Na+}{}_{HB}$, respectively). Given are instantaneous values at t = 120 ns (purple) together with mean values (blue dashed) and standard deviations (red and yellow dashed.), averaged over 120 ± 20 ns. Bottom: instantaneous vibrational frequencies of asymmetric $(PO_2)^-$ modes ν_{P1} as function of base step location for t = 120 ns.

The blue shifted ν_{P1} derived from QM/MM simulations indicate that the complete ensemble of simulated ν_{P1} frequencies along the RNA helix is not fully consistent with the observed IR spectrum (Fig. 1). Possible reasons for the discrepancy are (i) inherent limitations of force fields, (ii) shortcomings of the quantal QM/MM ansatz and (iii) insufficient equilibration of ion atmosphere around RNA. In particular convergence of ion atmosphere around DNA and RNA helices is challenging in MD simulations. Various equilibration time scales have been reported for DNA, ranging from tens of nanoseconds[14,15] (i.e. substantially slower equilibration than intra-helical structural quantities) to hundreds of nanoseconds[16,17,18] and substantial uncertainty prevails on equilibration periods of ion atmospheres around RNA.[19,20,21] As such dissecting shortcomings of insufficient equilibration from force field artifacts represents a formidable challenge in MD simulations.

In order to mitigate uncertainties due to equilibration and inherent limitations of the force field we further focus on a subset of $(PO_2)^-$ sites that shows P1 stretch frequencies $\nu_{P1} < 1250$ cm^{-1}. Figure S7 presents the IR spectra averaged over all realizations showing $\nu_{P1} < 1250$ cm^{-1} (red line, 41 realizations) that is compared to the IR signal obtained by averaging over all 1188 realizations (dashed purple line). We note that the criterion $\nu_{P1} < 1250$ cm^{-1} here serves to select particular $(PO_2)^-$ groups and adjacent ribose moieties along the RNA helix and all modes of such local sites contribute to the averaged IR signal.

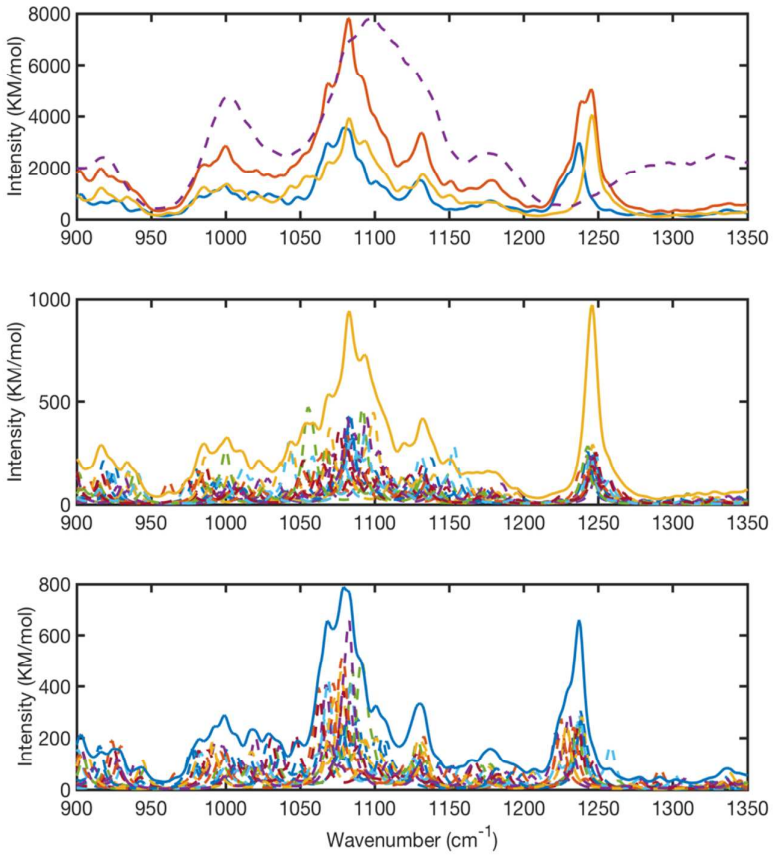

Fig. S7. Top: IR spectra averaged over all 1188 QM/MM normal mode simulations of $(PO_2)^-$ – ribose moieties (purple dashed line). Energy filtering ($\nu_{P1} < 1250$ cm^{-1}, red) reveals the double peak structure of ν_{P1} that can be further decomposed according to 1240 $cm^{-1} < \nu_{P1} <$ 1250 cm^{-1} (yellow) and $\nu_{P1} < 1240$ cm^{-1} (blue). Middle: contribution of 21 selected $(PO_2)^-$ – ribose moieties (1240 $cm^{-1} < \nu_{P1} < 1250$ cm^{-1}). Bottom: contribution of 18 selected $(PO_2)^-$ – ribose moieties ($\nu_{P1} < 1240$ cm^{-1}).

We find that the P1 region of the unfiltered IR spectrum is broad and diffuse, stretching out to > 1300 cm^{-1}. In contrast, the energy filtered IR signal ($\nu_{P1} < 1250$ cm^{-1}) shows a double peak structure in the P1 stretch region ($\nu_{P1}^{(1)} = 1246$ and $\nu_{P1}^{(2)} = 1237$ cm^{-1}), in good agreement to experiment and frequency position is determined by the neat water solvation environment.

Distinct vibrational frequencies are identified at 1131 cm^{-1}, with a shoulder at 1138 cm^{-1}, a triplet structure at 1093, 1083, 1068 cm^{-1}, and a low frequency doublet at 1000 and 986 cm^{-1}, allowing for clear assignment of vibrational bands observed in the experiment (cf. Table 1, Table S2 and Fig. S8). Further energetic filtering according to 1240 $cm^{-1} < \nu_{P1} < 1250$ cm^{-1} and $\nu_{P1} < 1240$ cm^{-1} allows to reveal the contribution of two subpopulations that impose the double peak structure of the P1 mode (Fig. S7, blue and yellow). Concerning the 1160 – 1200 cm^{-1} frequency range with increased intensity, compared to the experiment, we note that the spatial restriction to one $(PO_2)^-$ group with two adjacent ribose units in QM/MM normal mode simulations leads to an artificial enhancement of C-C stretch and C-H rocking modes by a factor of ~ 2 that particularly contribute in this spectral region. For the investigated Setups **A-C** we find that after the extended equilibration period of 39.4 ns differences in initial ion distribution are negligible and solvation structures of both water models appear comparable (see also Ref. 20) justifying the averaging for IR spectra over the three considered setups.

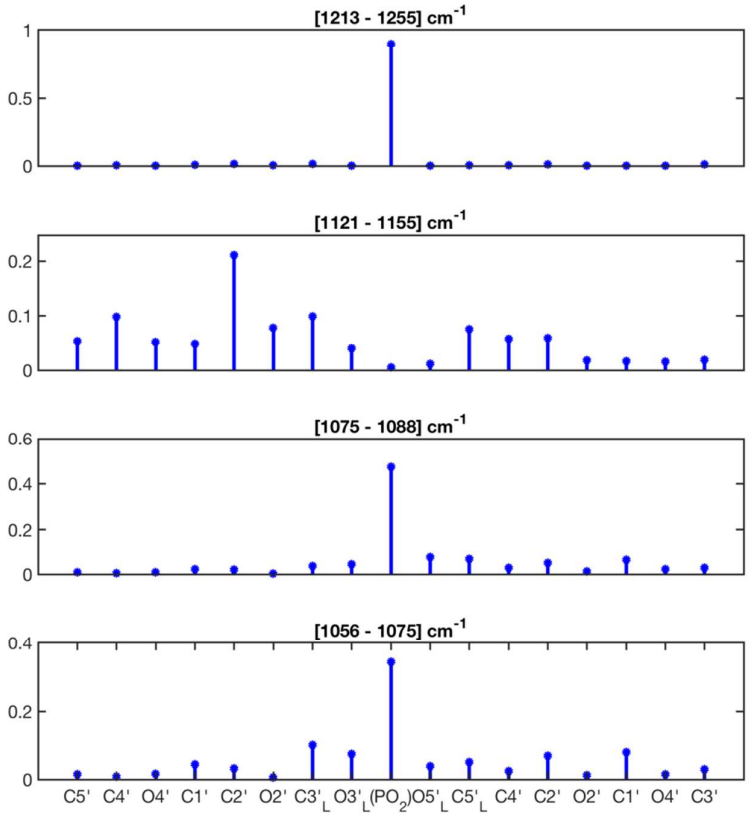

Fig. S8. Normalized mass and intensity weighted average atomic displacements of indicated frequency regions employed for assignment of phosphate-backbone vibrational frequencies (cf. Table 1 and Table S1). Shown are (from top to bottom) mass and intensity weighted displacements of asymmetric $(PO_2)^-$ stretch ($\nu_{P1}^{(1)}$ and $\nu_{P1}^{(2)}$), C_2'-O_2'-H stretch ($\nu_{C2'\text{-}OH}$) with overlapping contributions of ribose C_1'-O_4'-C_4' stretch ($\nu_{C\text{-}O\text{-}C}$), symmetric $(PO_2)^-$ stretch (ν_{P2}) and linker C-O stretch (ν_{L2}).

Visual inspection of normal mode vectors reveals that the majority of normal modes poses strongly delocalized character where mode mixing and atomic displacements vary with particular realizations along the RNA double helix and instantaneous solvation structure. Assignment of vibrational modes is thus performed with help of the mass and intensity weighted magnitude squared of respective atomic displacements within a given energy interval, averaged over the particular realizations with $\nu_{P1} < 1250$ cm^{-1} (Table S1 and Fig. S8, cf. dashed lines in Fig. S7). Here mass weighting highlights localized displacements of functional group heavy atoms compared to light hydrogen atoms and intensity weighting accounts for the contribution of particular modes to the observable IR signal. To further assess mode mixing of ν_{P1} with the δ(C2'-OH) bending mode (cf. Ref. 22) we further consider the intensity weighted magnitude squared of respective atomic displacements (data not shown), revealing significant mixing of functional groups (42 % $(PO_2)^-$, 22 % C2'-OH, 21 % C3'-O3') in normal mode eigenvectors where high intensity in the 1220-1240 cm^{-1} range of particular realizations is determined by the ν_{P1} mode. The displacements of eigenvectors are sensitive to particular realizations of C2'-OH …. OH_2 hydrogen bond.

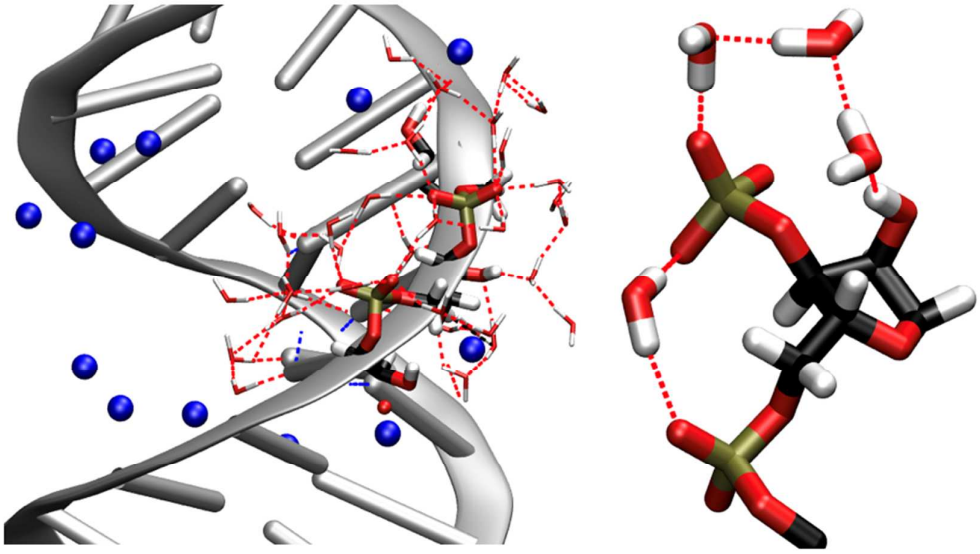

Fig. S8. Solvation structure of base step # 7-8 (cf. Fig. S6) with counterions shown in blue. The magnification (right) highlights a $(PO_2)^-$…$(PO_2)^-$ bridging water molecule and a hydrogen bond network ring structure mediated by the C2'-OH group as discussed in the main text.

References

(1) Siebert, T.; Guchhait, B.; Liu, Y.; Costard, R.; Elsaesser, T. Anharmonic Backbone Vibrations in Ultrafast Processes at the DNA−Water Interface. *J. Phys. Chem. B* **2015**, *119*, 9670−9677.

(2) Guchhait, B.; Liu, Y.; Siebert, T.; Elsaesser, T. Ultrafast Vibrational Dynamics of the DNA Backbone at Different Hydration Levels Mapped by Two-Dimensional Infrared Spectroscopy. *Struct. Dyn.* **2016**, *3*, 043202.

(3) Siebert, T.; Guchhait, B.; Liu, Y.; Fingerhut, B. P.; Elsaesser, T. Range, Magnitude, and Ultrafast Dynamics of Electric Fields at the Hydrated DNA Surface. *J. Phys. Chem. Lett.* **2016**, *7*, 3131−3136.

(4) Khalil, M; Demirdoven, N; Tokmakoff, A. Coherent 2D IR spectroscopy: Molecular Structure and Dynamics in Solution. *J. Phys. Chem. A* **2003**, *107*, 5258-5279.

(5) Levinger, N. E.; Costard, R.; Nibbering, E. T. J.; Elsaesser, T. Ultrafast Energy Migration Pathways in Self-Assembled Phospholipids Interacting with Confined Water. *J. Phys. Chem. A* **2011,** *115***,** 11952-11959.

(6) Case, D.A.; Babin, V.; Berryman, J.T.; Betz, R.M.; Cai, Q.; Cerutti, D.S.; Cheatham, III, T.E.; Darden, T.A.; Duke, R.E.; Gohlke, H.; Goetz, A.W.; Gusarov, S.; Homeyer, N.; Janowski, P.; Kaus, J.; Kolossváry, I.; Kovalenko, A.; Lee, T.S.; LeGrand, S.; Luchko, T.; Luo, R.; Madej, B.; Merz, K.M.; Paesani, F.; Roe, D.R.; Roitberg, A.; Sagui, C.; Salomon-Ferrer, R.; Seabra, G.; Simmerling, C.L.; Smith, W.; Swails, J.; Walker, R.C.; Wang, J.; Wolf, R.M.; Wu, X.; Kollman, P.A. AMBER 14, **2014**, University of California, San Francisco.

(7) Perez, A.; Marchan, I.; Svozil, D.; Sponer, J.; Cheatham, III, T.E.; Laughton, C.A.; Orozco, M. Refinement of the AMBER Force Field for Nucleic Acids: Improving the Description of alpha/gamma Conformers. *Biophys. J.* **2007**, *92*, 3817–3829.

(8) Joung, I.S.; Cheatham, III, T.E. Determination of Alkali and Halide Monovalent Ion Parameters for Use in Explicitly Solvated Biomolecular Simulations. *J. Phys. Chem. B* **2008**, *112*, 9020–9041.

(9) Joung, I.S.; Cheatham, III, T.E. Molecular Dynamics Simulations of the Dynamic and Energetic Properties of Alkali and Halide Ions using Water-Model-Specific Ion Parameters. *J. Phys. Chem. B* **2009**, *113*, 13279–13290.

(10) Salomon-Ferrer, R.; Götz, A. W.; Poole, D.; Le Grand, S.; Walker, R. C. Routine Microsecond Molecular Dynamics Simulations with AMBER on GPUs. 2. Explicit Solvent Particle Mesh Ewald. *J. Chem. Theory Comput.* **2013**, *9*, 3878-3888.

(11) Le Grand, S.; Götz, A. W.; Walker, R. C. SPFP: Speed without Compromise - A Mixed Precision Model for GPU accelerated molecular dynamics simulations. *Comput. Phys. Commun.* **2013**, *184*, 374-380.

(12) Valiev, M.; Bylaska, E.J.; Govind, N.; Kowalski, K.; Straatsma, T.P.; van Dam, H.J.J.; Wang, D.; Nieplocha, J.; Apra, E.; Windus, T.L.; de Jong, W.A. NWChem: A Comprehensive and Scalable Open-Source Solution for Large Scale Molecular Simulations. *Comput. Phys. Commun.* **2010**, *181*, 1477-1489.

(13) Grimme, S.; Antony, J.; Ehrlich, S.; Krieg, H. A Consistent and Accurate Ab-Initio Parametrization of Density Functional Dispersion Correction (DFT-D) for the 94 Elements H-Pu. *J. Chem. Phys.* **2010**, *132*, 154104.

(14) Ponomarev, S. Y.; Thayer, K. M.; Beveridge, D. L. Ion Motions in Molecular Dynamics Simulations on DNA. *Proc. Natl. Acad. Sci. USA* **2004**, *101*, 14771-14775.

(15) Yoo, J.; Aksimentiev, A. Competitive Binding of Cations to Duplex DNA Revealed through Molecular Dynamics Simulations. *J. Phys. Chem. B* **2012**, *116*, 12946-12954.

(16) Pasi, M.; Maddocks, J. H.; Lavery, R.; Analyzing Ion Distributions around DNA: Sequence-Dependence of Potassium Ion Distributions from Microsecond Molecular Dynamics. *Nucleic Acids Res.* **2015**, *43*, 2412-2423.
(17) Drozdetski, A. V.; Tolokh, I. S.; Pollack, L.; Baker, N.; Onufriev, A. V. Opposing Effects of Multivalent Ions on the Flexibility of DNA and RNA. *Phys. Rev. Lett.* **2016**, *117*, 028101.
(18) Dans, P. D.; Danilane, L.; Ivani, I.; Drasata, T.; Lankas, F.; Hospital, A.; Walther, J.; Pujagut, R. I.; Battistini, F.; Gelpi, J. L.; Lavery, R.; Orozco, M. Long-Timescale Dynamics of the Drew-Dickerson Dodecamer. *Nucleic Acids Res.* **2016**, *44*, 4052-4066.
(19) Pan, F.; Roland, C.; Sagui, C.; Ion Distributions around Left- and Right-Handed DNA and RNA Duplexes: A Comparative Study. *Nucleic Acids Res.* **2014**, *42*, 13981-13996.
(20) Kuehrova, P.; Otyepka, M.; Sponer, J.; Banas, P.; Are Waters around RNA More than Just a Solvent? - An Insight from Molecular Dynamics Simulations. *J. Chem. Theory and Comput.* **2014**, *10*, 401-411.
(21) Besseova, I.; Banas, P.; Kuhrova, P.; Kosinova, P.; Otyepka, M.; Sponer, J. Simulations of A-RNA Duplexes. The Effect of Sequence, Solute Force Field, Water Model, and Salt Concentration. *J. Phys. Chem. B* **2012**, *116*, 9899-9916.
(22) Kolkenbeck, K.; Zundel, G. The Significance of the 2' OH Group and the Influence of Cations on the Secondary Structure of the RNA Backbone. *Biophys. Struct. Mech.* **1975**, *1*, 203-219.
(23) Tsuboi, M. Application of Infrared Spectroscopy to Structure Studies of Nucleic Acids. *Appl. Spectrosc. Rev.* **1970**, *3*, 45-90.
(24) Banyay, M.; Sarkar, M.; Gräslund, A. A Library of IR Bands of Nucleic Acids in Solution. *Biophys. Chem.* **2003**, *104*, 477−488.
(25) Lindqvist, M.; Sarkar, M.; Winqvist, A.; Rozners, E.; Strömberg, R.; Gräslund, A. Optical Spectroscopy Study of the Effects of a Single Deoxyribose Substitution in a Ribose Backbone: Implications in RNA-RNA Interaction. *Biochemistry* **2000**, *39*, 1693-1701.

Table S1: Backbone modes of RNA. Average mode character with assignment from mass and intensity weighted magnitude of atomic displacements (cf. Fig. S8). Frequency intervals (in cm^{-1}) as indicated by square brackets.

Mode	Assignment	Exp. /cm^{-1}	Theory /cm^{-1}	Character. /%	Ref. [22]	Ref. [23]	Ref. [24,25]
$\nu_{P1}^{(1)}$	asymmetric $(PO_2)^-$ stretch	1247	1246 [1255-1240]	87.9 $(PO_2)^-$	$(PO_2)^-$	-	$(PO_2)^-$ A-form
$\nu_{P1}^{(2)}$	asymmetric $(PO_2)^-$ stretch; minor $\delta(C_2\text{-}OH)$	1220	1237 [1240-1213]	91.2 $(PO_2)^-$	$(PO_2)^-$ $\delta(C_2\text{-}OH)$	$(PO_2)^-$	Ribose sugar
$\nu_{C\text{-}O\text{-}C}$	Ribose $C_{1'}\text{-}O_{4'}\text{-}C_{4'}$ stretch	1133	1138 [1155-1135]	37.7 C_2-OH 28.7 $C_{1'}\text{-}O_{4'}\text{-}C_{4'}$	C_2-OH	C_2-OH	Ribose C1'C2'OC3'
$\nu_{C2\text{-}OH}$	C_2-OH stretch	1120	1131 [1135-1121]	36.1 C_2-OH 29.0 $C_{1'}\text{-}O_{4'}\text{-}C_{4'}$		C_2-OH	Ribose C1'C2'OC3'
ν_{L1}	Linker C-O stretch	1102	1093 [1113-1089]	20.8 $C\text{-}O^{L1/2}$ 40.0 $(PO_2)^-$		-	-
ν_{P2}	symmetric $(PO_2)^-$ stretch	1087	1083 [1088-1075]	47.5 $(PO_2)^-$ 22.5 $C\text{-}O_{L1/2}$	$(PO_2)^-$ stretch	$(PO_2)^-$ stretch	symmetric $(PO_2)^-$ stretch
ν_{L2}	Linker C-O stretch	1062	1068 [1175-1056]	24.2 $C\text{-}O^{L1/2}$ 34.4 $(PO_2)^-$	O-C-O	-	Linker C-O stretch
$\nu_{CC\text{-}OC}$	Ribose $C_{1'}\text{-}O_{4'}\text{-}C_{4'}$ stretch, Ribose $C_{3'}\text{-}C_{4'}$ stretch	994	1000 [1010-991]	40.7 $C_{1'}\text{-}O_{4'}\text{-}C_{4'}$ 24.7 $C\text{-}O^{L1/2}$		-	Ribose
$\nu_{C\text{-}C}$	$C_{4'}\text{-}C_{5'}$ ethyl-stretch	970	986 [991-971]	27.1 $C_{4'}\text{-}C_{5'}$ 29.4 $C_{1'}\text{-}O_{4'}\text{-}C_{4'}$ 40.8 $C\text{-}O^{L1/2}$		C-C (DEP)	RNA backbone